# Fracture Analysis of the Cathode in Li-Ion Batteries: A Simulation Study

M. Zhu, J. Park and A. M. Sastry

*J. Electrochem. Soc.* 2012, Volume 159, Issue 4, Pages A492-A498.
doi: 10.1149/2.045204jes

*Journal of The Electrochemical Society*, **159** (4) A492-A498 (2012)
0013-4651/2012/159(4)/A492/7/$28.00 © The Electrochemical Society

# Fracture Analysis of the Cathode in Li-Ion Batteries: A Simulation Study

**M. Zhu,[a] J. Park,[a] and A. M. Sastry[a,b,c,z]**

[a]*Department of Mechanical Engineering,* [b]*Department of Material Science Engineering, and*
[c]*Department of Biomedical Engineering, University of Michigan, Ann Arbor, Michigan 48109, USA*

In order to achieve a high level of reliability in rechargeable Li-ion batteries, battery cell materials must maintain good mechanical stability over many cycles. Stresses due to intercalation, phase transition, and thermal loading can cause local fractures in the active materials of Li-ion batteries, as has been experimentally observed. The resulting fracture of the cathode materials is one putative degradation mechanism of Li batteries; it inevitably results in a loss of electrical contact and an increase in the surface area for active material dissolution and SEI layer formation. In this work, we investigate the conditions under which initial defects propagate and form larger fractures in the cathode material ($LiMn_2O_4$) during the charging and discharging cycles of electrochemical reactions. Fracture analysis based on the extended finite element method (XFEM) is used to evaluate the effects of current density, particle size and particle aspect ratio on the propagation of defects. Both current density and particle size are shown to be positively correlated with fracture propagation, though not monotonically so in the case of aspect ratio. With an aspect ratio of 1.5:1, a particle with a defect at the center will crack at a low C-rate; this case is one of the most severe among all aspect ratios.
 [DOI: 10.1149/2.045204jes] 

Manuscript submitted July 25, 2011; revised manuscript received January 6, 2012. Published February 9, 2012.

The potential market size for both electric and hybrid electric vehicles is enormous, but growth will require the development of longer useful lifetimes of Li-ion batteries, particularly in aggressive operating conditions. The current challenge in making batteries that are longer-lasting and more cost-effective relative to vehicle life cycle is reducing capacity fade. A number of causes are postulated to contribute to capacity fade, including electrochemical, chemical, and mechanical degradation, of which fracture is a part.

Fracture of active material particles and conductive aggregates causes separation of particle fragments and isolation of the electronically conducting matrix, resulting in loss of electric contact.[1,2] Fracture of active material particles also increases the surface area exposed to the electrolyte, thus increasing side-reactions and $Mn^{2+}$ dissolution[3,4] into the electrolyte as well as accelerating capacity fade, especially at elevated temperature. The development and propagation of fractures at the particle and aggregate level can also affect the mechanical stability of Li-ion battery materials. It remains unknown, however, how fractures develop and propagate at different length scales in the battery material, as well as the extent to which local fractures limit battery lifetime.

Local fractures have been experimentally observed in several cathode materials for Li-ion batteries.[2,5,6] Scanning electron microscope (SEM) images[5] have shown evident disruption in the surface of Li/Au-codeposited $LiMn_2O_4$ particles with a diameter of 20 $\mu$m cycled at a scan rate of 4 mV/s, whereas no fracture was observed for a smaller scan rate of 0.1 mV/s. This indicates that the propensity of fracture is related to current level and that fracture is more likely to occur during cycling at a higher C-rate. Experimentally,[2] the capacity of a $LiFePO_4$, cells have been shown to fade gradually from the initial 149 mAh/g to 117 mAh/g with a current density of 30 mA/g at room temperature after 60 cycles. Both SEM and transmission electron microscope (TEM) techniques have been used to characterize the $LiFePO_4$ particles, and it has been shown that the particles cracked during cycling, possibly due to the high internal strain. The fracture of $LiFePO_4$ was proposed as one of the reasons for capacity fading in the cell under experiment. In other experimental work,[6] $LiCoO_2$ particles were cycled 50 times between 2.5 and 4.35 V at a current density of 0.4 mA/cm$^2$. TEM results showed that local microstructural and crystallograhic changes had occurred, although the cell was still electrochemically stable. Accumulated damage of this kind was proposed to be responsible for degradation in $LiCoO_2$-based batteries upon overcharging or after extended cycling. Fracture in $LiMn_2O_4$ particles has also been observed using various other techniques, including X-ray diffraction (XRD)[7,8] and acoustic emission spectroscopy.[9]

One possible cause of fracture in battery materials is high stress. Stress can be induced in battery materials during fabrication, which usually involves compression to control the porosity of the cathode[10–12]; it can also result from cycling of the cells throughout the lifetime of the Li-ion batteries due to the intercalation of lithium ions as well as the transition of active material phases. In $Li_xMn_2O_4$ spinel systems, where $0 < x < 1$, lithium is inserted into and extracted from the interstitial sites in the host $Mn_2O_4$ framework, resulting in the expansion and contraction of the cubic lattice structure.[13,14] A 6.5% volume change in the cubic phase of $Li_xMn_2O_4$ results from the intercalation of Li-ions when x changes from 0.2 to 0.995.[13] An even larger volume change and stress level increase can be introduced by phase transition, at which time the $Li_xMn_2O_4$ material is further lithiated to $1 < x < 2$, and Jahn-Teller distortion occurs, resulting in 5.6% total expansion in unit cell volume.[15,16] The stress caused by both the first order transition and Jahn-Teller distortion can contribute to local fracture in the active material of a battery cathode.

Several models have been developed to determine the stress generated by lithium intercalation and deintercalation. One-dimensional models[17,18] have been developed to estimate stress generation in spherical electrode particles. Three-dimensional finite element simulations have also been developed to model the diffusion-induced stress in analogy to thermal stress,[19,20] and relationships have been established between stress levels within cathode particles and parameters such as current density, voltage and particle size. Analytical expressions have been constructed to capture the stress evolution in spherical electrode particles under galvanostatic or potentiostatic conditions[21–23] in an attempt to determine which operating conditions prevent cracking in electrodes. Stress generated in spherical particles that consider both diffusion and phase transition is calculated analytically and used to predict fracture.[24] A lithium insertion induced fracture mechanism was employed in $LiFePO_4$ materials to predict cracking in two electrode phases, without considering realistic particle geometry.[25] Further[26] an "electrochemical shock" model has also been proposed to calculate the conditions under which crack propagation develops from an initial semicircular defect on the surface of a spherical electrode particle. In this model the driving force for the initial defect to crack is a tensile tangential stress at the particle surface.

However, no direct relationship between stress and fracture has been established for ellipsoidal particles of aspect ratios other than one, which are capable of more general and realistic cases for electrode particles. The geometric and electrochemical conditions under which initial defects further propagate and form larger fractures

[z] E-mail: amsastry@umich.edu

in the cathode materials under electrochemical reactions during charge/discharge cycles remains to be investigated. In our present work, our objectives are as follows:

1) determine the effect of current density on the state of stress;
2) determine the effect of particle shape and size on the state of stress;
3) for both spherical and ellipsoidal particles, determine the range of the above mentioned parameters under which the states of stress will result in fracture propagation; and
4) determine the effect of the initial defect location on fracture propagation.

## Methods

Tensile stress is correlated to fracturing in cathode particles (in this case, the brittle material $LiMn_2O_4$) during cycling. In order to determine the conditions under which crack propagation occurs, three principal stresses $\sigma_1$, $\sigma_2$, and $\sigma_3$ were calculated using COMSOL Multiphysics simulation for particles without an initial defect during cycling. Their evolution during lithium intercalation and deintercalation was also captured. The three principal stresses were ranked in descending order, and the largest of the three—maximum principal stress—was denoted $\sigma_1$. In each case, the highest point of $\sigma_1$ was identified in the particle and the maximum principal stress at that location was denoted $\sigma_{1,MAX}$ · $\sigma_{1,MAX}$ rose to its peak before the charge/discharge process reached its end due to the reduction of the Li-ion concentration gradient in the later stage. The stress states when $\sigma_{1,MAX}$ peaks were used in fracture simulations so as to capture the most severe conditions for crack propagation. These peak $\sigma_{1,MAX}$ in different simulation cases were ranked, and only the cases in which peak $\sigma_{1,MAX}$ exceeded 70% of the maximum tensile strength of $LiMn_2O_4$ were selected for further fracture simulation with ABAQUS. The threshold of 70% max tensile strength was selected to filter out the cases where crack propagation was unlikely. The fracture simulation used the calculated Li-ion concentration profile as an input to evaluate the stress state for particles with initial defects and determine whether crack propagation occurs.

Section 2.1 provides the governing equations and methodologies used in the 3D finite element analysis in this study; Section 2.2 explains the simulation setups and the range of parameters under study; and Section 2.3 describes the material properties used in the simulation.

*Three-dimensional finite element simulation.*— During the discharge of Li-ion cells, lithium inserts itself into the $Mn_2O_4$ host structure and occupies open tetrahedral sites. The diffusion of lithium into the $Mn_2O_4$ particle forms a concentration gradient profile that results in a stress field in the cubic $Li_xMn_2O_4$ phase. In this work, it was assumed that only a single cubic phase of $Li_xMn_2O_4$ existed in the particle, where $0 < x < 1$. The volume change in a single phase particle was solely attributable to the insertion and extraction of lithium to and from the interstitial sites in the $Mn_2O_4$ framework. In the simulations conducted, it was assumed that the onset of Jahn-Teller distortion in the spinel structure was prevented by charging and discharging the cell between $x = 0$ and $x = 1$ only.

The lithium intercalation-induced stress during cycling was calculated using an analogy to thermal stress,[19,20,27] assuming that the lattice constants of the material changed linearly with the amount of ions inserted.[13]

To obtain the concentration profile due to intercalation, the diffusion problem was solved together with the elastic field. The driving force for Li-ion diffusion can be obtained by the gradient of the characteristic potential comprising the chemical and elastic energy of the system. The diffusion flux $\mathbf{J}$ is given by[19]

$$\mathbf{J} = -D\left(\nabla c - \frac{\Omega c}{RT}\nabla\sigma_h\right) \quad [1]$$

where $c$ is the concentration of the Li-ions, $D$ is the diffusion coefficient, $\Omega$ is the partial molar volume of Li-ion, $R$ is a gas constant, $T$ is absolute temperature, and $\sigma_h$ is the hydrostatic stress.

Combining Eq. 1 with the mass conservation equation, $\partial c/\partial t + \nabla\cdot\mathbf{J} = 0$, we have

$$\frac{\partial c}{\partial t} = D\left(\nabla^2 c - \frac{\Omega}{RT}\nabla c\cdot\nabla\sigma_h - \frac{\Omega c}{RT}\nabla^2\sigma_h\right) \quad [2]$$

The initial condition is $c = c_o$, and the constant current boundary condition

$$\mathbf{J} = -D\left(\nabla c - \frac{\Omega c}{RT}\nabla\sigma_h\right) = \frac{\mathbf{i_n}}{F} \quad [3]$$

where $\mathbf{i}_n$ is the current density on the particle surface and $F$ is Faraday's constant.

The stress-strain relation with the existing concentration gradients can be written as

$$\varepsilon_{ij} = \frac{1}{E}[(1+\upsilon)\sigma_{ij} - \upsilon\sigma_{kk}\delta_{ij}] + \frac{\tilde{c}\Omega}{3}\delta_{ij} \quad [4]$$

where $\tilde{c} = c - c_0$ is the lithium concentration change from the original stress-free value, $\varepsilon_{ij}$ and $\sigma_{ij}$ are strain and stress components, $E$ is Young's modulus, $\upsilon$ is Poisson's ratio, c is the Li-ion concentration, and $\delta_{ij}$ is the Kronecker delta. The last term accounts for the intercalation strain.

The problem was solved in three-dimensional space using FEMLAB (COMSOL Multiphysics). Two models were included in the multiphysics simulation: the PDE (partial differential equation) model and the solid stress–strain model. In the PDE model, the diffusion process was described by the generalized form of Eq. 2. In the solid stress–strain model, "thermal expansion" was included as a load based on the variable of the concentration $c$ instead of temperature in the thermal stress calculation.

The calculated Li-ion concentration profile was then exported to a fracture simulation model as an input condition. The fracture propagation was simulated using ABAQUS 6.9 standard with Extended Finite Element Method (XFEM), in which the elements that contained cracks were enriched[28]: the singularity around the tip of the crack was captured by the near-tip asymptotic functions and the discontinuous jump in displacement across the crack surfaces was represented by a discontinuous function. Fracturing was simulated with a damage initiation rule based on maximum principal stress criterion, followed by a damage evolution rule which considers the energy required for fracture to extend beyond the initiation of damage.

*Design of experiments.*— In this study, the effects of current density, particle size and particle shape on the stress state were investigated; whether or not the peak state of stress during charging/discharging resulted in fracture propagation was determined; and the effect of initial defect location on crack propagation was also examined.

*Stress evolution.*—To find the evolution of the state of stress during cycling, a spherical particle with a radius of 7 μm and without initial defect was subjected in the COMSOL Multiphysics simulation to both a charging and then a discharging process. The surface current density was set to be 0.5 A/m$^2$ in both cases. The $\sigma_{1,MAX}$ was plotted against charge/discharge time.

*Particle size and current density.*—Particle size and current density were considered two key parameters in this study because 1) variation of current density affects concentration gradient, which in turn affects the amount of volume expansion; and 2) variation in size also affects the amount of volume expansion, which in turn determines the stress level inside a particle. This study focused on the discharge process because discharging rates for Li-ion batteries are often higher than the charging rates in real world applications per manufacturer recommendations and thus require more attention. The radii of the spheres ranged from 3 μm to 9 μm, in 1 μm increments. For each particle radius, the surface current density was varied from 0.1 A/m$^2$ to 0.6 A/m$^2$, with an increment of 0.1 A/m$^2$. For each case, the peak $\sigma_{1,MAX}$ was found for particles without defect via COMSOL and the calculated Li-ion concentration profiled was exported to the ABAQUS

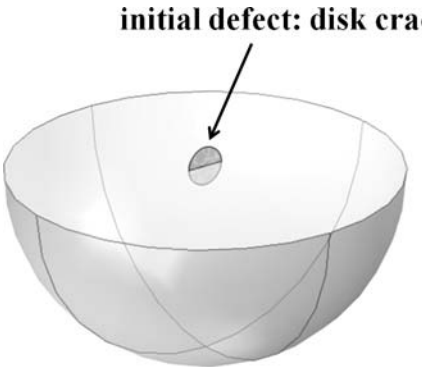


**Figure 1.** Position of initial defect in a $Mn_2O_4$ particle.

fracture simulation. In the ABAQUS model, the initial crack was disk-shaped with a diameter 1/10 of that of the sphere; it was located in the center of the particle as shown in Figure 1, where the highest maximum principal stress was found during discharge. The range of these parameters is summarized in Table I.

*Particle aspect ratio.*—Besides these two parameters, aspect ratio (α) is also an important geometric factor that affects the stress level of $Mn_2O_4$ particles.[19,20,29] Since the real battery electrodes are generally composed of irregularly shaped particles, ellipsoidal particles with aspect ratios other than one are more general and more realistic representations of irregular electrode particles. In order to study the effect of particle aspect ratio and surface current density on fracture propagation, particles with aspect ratios ranging from 1 to 4 were simulated. The shape of the particles was prolate ellipsoid with two semi-minor axes of equal length and a longer semi-major axis. The aspect ratio α was defined as the ratio of the semi-major axis and the semi-minor axes. In order to keep the capacity of the active material constant, the total volume of the particles was fixed at $4\pi \times (7\,\mu m)^3/3$. Current density was varied. However, for different aspect ratios, the total surface current (the product of the current density and the surface area) was conserved at each level. The increment of total surface current was fixed at 0.2 A/m$^2$ $\times 4\pi \times (7\,\mu m)^2$. Therefore, the C-rate at each level was kept constant across particles of varying aspect ratio. The C-rates ranged from 0.07 C to 0.42 C, with an increment of 0.07 C. For each case, the peak $\sigma_{1,MAX}$ was found for particles without defect via COMSOL and the calculated Li-ion concentration profiled was exported to the ABAQUS fracture simulation. In the ABAQUS model, the initial crack was disk- shaped with a diameter 1/10 of that of the semi-minor axis of the ellipsoidal particle; it was located at the center of the particle. The range of the parameters is summarized in Table I.

*Initial defect location.*—Finally, the initial defect location is another important factor, since in the actual material defects may exist at any location throughout the volume of a particle. To investigate the effect of initial defect location on fracture propagation, the position of the initial defect in a particle $4\pi \times (7\mu m)^3/3$ in volume and with aspect ratio 2 was relocated from the center of the particle to the surface of the particle. Depending on the direction of Li-ion flow, the maximum stress could be located at the center of a particle, at the surface, and at the end of the shortest axis, which implies that both the charging and discharging processes should be examined for initial defect locations over the whole volume of the particle. Thus for each initial defect location, the particle was subjected to both the charging and the discharging process, and in each case the C-rate was varied from 0.07C to 0.42 C, with an increment of 0.07 C. The lowest C-rate at which fracture propagation occurred was reported.

**Table II. Material properties $Mn_2O_4$.**

| Property | Unit | $Mn_2O_4$ |
|---|---|---|
| Young's modulus ($E$) | GPa | 100[32–34] |
| Poisson's ratio ($\upsilon$) | | 0.3[27] |
| Diffusion coefficient ($D$) | m$^2$/s | $7.08 \times 10^{-15}$[19] |
| Stoichiometric maximum concentration ($c_{max}$) | mol/m$^3$ | $2.29 \times 10^4$[36] |
| maximum tensile strength ($\sigma_{TS}$) | MPa | 100[24,35] |
| surface energy ($\gamma$) | J/m$^2$ | 0.66[25] |

*Material Properties.*— As seen in many engineering materials, the orientation of crystalline and grain microstructures are distributed randomly[30,31] so that macroscopic elastic properties are almost equal in all directions. Thus isotropic behavior was assumed, which was reasonable for the purpose of the present work.

The Young's modulus value for the exact material ($Mn_2O_4$) in the electrode from direct measurement was not readily available. Values reported in the literature on porous sintered polycrystalline samples and other spinel oxides ranged from 10 GPa to 300 GPa.[32–34] In this work, an estimated value of 100 GPa was used as Young's modulus.

Because maximum tensile strength for the exact material ($Mn_2O_4$) was not reported in the literature, this study estimated the maximum tensile strength based on the properties of similar brittle materials. For example, $TiO_2$, which is also an oxide and has a density similar to $Li_xMn_2O_4$ (4.24 g/cm$^3$ compared to 4.4–4.5 g/cm$^3$), had a tensile strength of 69-103 MPa.[35,24] The maximum tensile strength was estimated to be 100 MPa for $Mn_2O_4$ in the simulation. The surface energy was estimated from similar cathode material as 0.66J/m$^2$.[25]

Material properties are summarized in Table II.

## Results

*Stress evolution.*— For the spherical particle with radius 7 μm under study, $\sigma_{1,MAX}$ was found at the surface of the sphere during charge and at the center of the sphere during discharge. Figure 2 shows that in the spherical particle $\sigma_{1,MAX}$ increased monotonously during the charging process; it should be noted, however, that it first increased to its peak and subsequently decreased during the discharging process. The increase in the stress level during charging could be explained by the fact that the outer part of the particle experienced pressure due to a relatively higher rate of contraction compared to the inside of the particle when Li-ions de-intercalated through the surface. The decrease in the stress level after 960 seconds of discharging could be explained by the fact that as more Li-ions intercalated into the

**Table I. Simulation parameters.**

| Factors | Levels | | | | | | |
|---|---|---|---|---|---|---|---|
| particle radius | 3 μm | 4 μm | 5 μm | 6 μm | 7 μm | 8 μm | 9 μm |
| current density | 0.1A/m$^2$ -0.6A/m$^2$, with an increment of 0.1 A/m$^2$ (for each particle radius) | | | | | | |
| **Factors** | **Levels** | | | | | | |
| aspect ratio | 1:1 | 1.5:1 | 2:1 | 3:1 | 4:1 | | |
| C-rate | 0.07 C – 0.42 C, with an increment of 0.07C (for each aspect ratio) | | | | | | |

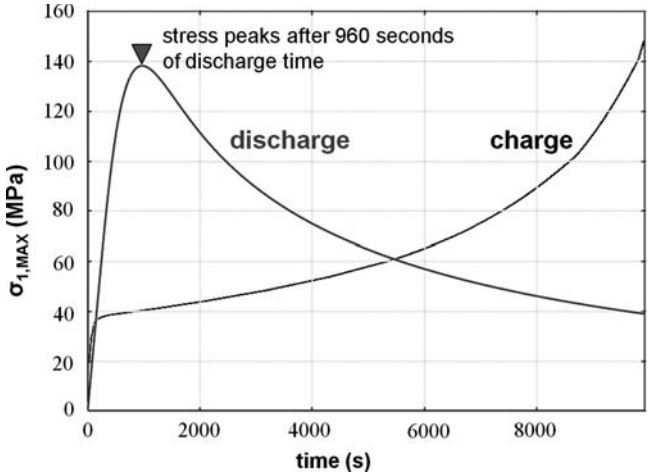


**Figure 2.** Evolution of $\sigma_{1,MAX}$ during the charging and discharging process for a spherical particle with a radius of 7 μm.

particle while the Li-ion concentration at the particle center rises, the concentration gradient decreased during the later stage of the discharge. It was further noted that the peak $\sigma_{1,MAX}$ values were similar during both the charging and discharging processes. In real battery applications, the discharge rate is often higher than the charge rate; thus, the current study focuses mainly on the discharging process.

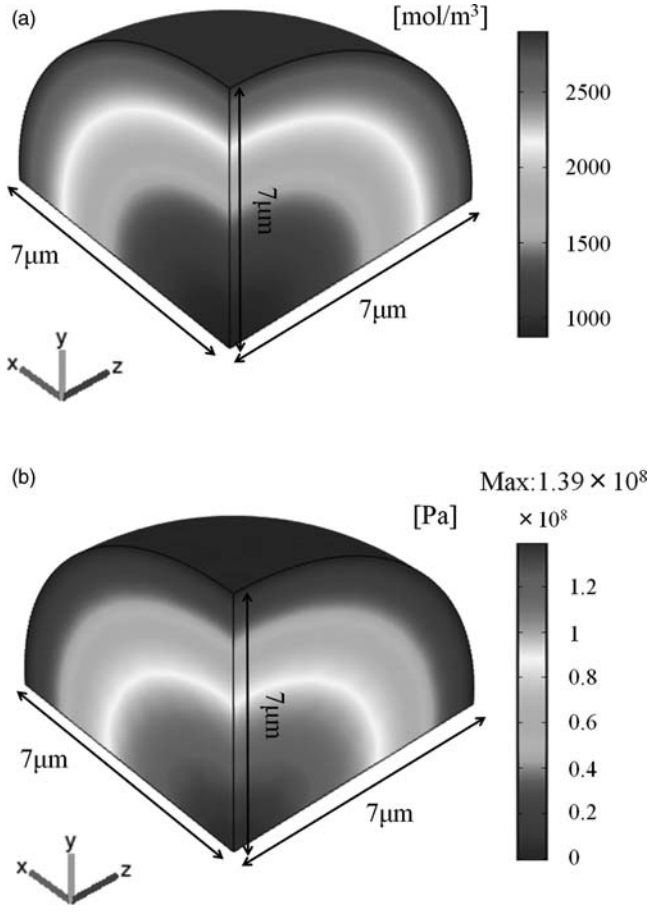


**Figure 3.** Lithium concentration profile and maximum principal stress in a spherical particle during the discharging process (radius = 7 μm, current density = 0.5A/m$^2$, discharge time = 960 seconds when $\sigma_{1,MAX}$ peaks) (a) lithium concentration [mol/m$^3$] (b) max. principal stress [Pa].

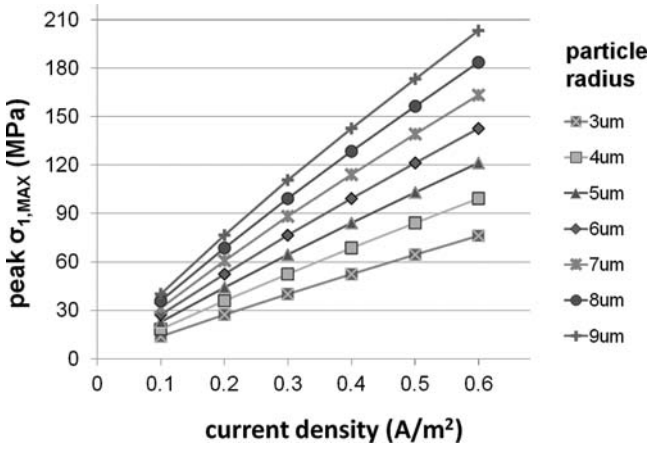


**Figure 4.** Peak $\sigma_{1,MAX}$ values for spherical particles.

*Particle size and current density.*— Figure 3a shows the concentration profile for a spherical particle with radius 7 μm and surface current density 0.5A/m$^2$ after a discharge time of 960 seconds. The concentration varied from low in the center of the particle to high on the particle surface, indicating higher expansion of the outer part of the particle. As a result, the difference in expansion rate subjected the material of the spherical particle to tensile stress in the direction normal to the sphere surface, creating a condition for mode I fracture to occur. Figure 3b shows the maximum principle stress level inside the particle, resulting from the difference in expansion rate caused by the Li-ion concentration gradient discussed above. The maximum principal stress was lower near the surface and higher near the center of the particle. The same phenomenon was observed for all the investigated particles with different sizes and aspect ratios. For fracture in brittle material such as $Mn_2O_4$, the maximum principal stress criterion gave reasonably accurate predictions. Thus, during discharge crack propagation was more likely to occur with the initial defect near the center of the particle (which was confirmed by changing the initial defect location in a later section); one would miss important phenomena in the fracture study if the inside of the particle were not investigated. The peak $\sigma_{1,MAX}$ for each simulation case for spherical particles is plotted in Fig. 4. The simulation revealed whether initial defects in the center of the particles propagated further; the results are mapped out in Fig. 5, and a critical boundary was plotted. The small blue

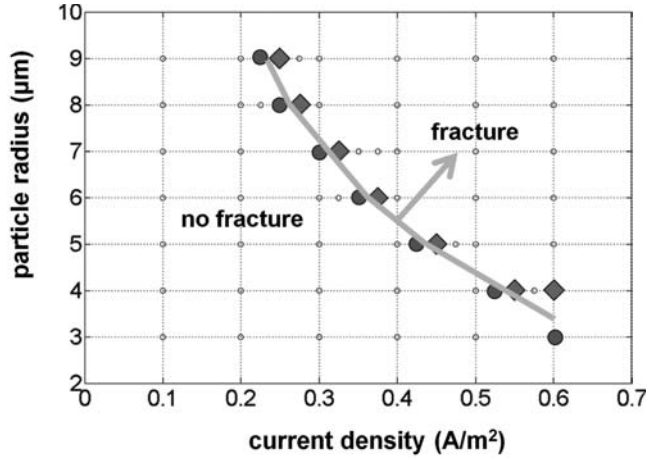


**Figure 5.** Fracture propagation conditions (particle size and current density). The small blue circles represent all cases simulated, whereas the large blue dots (denoting the absence of crack propagation) and red diamonds (denoting crack propagates) represent cases located closest to the critical boundary (shown in green).

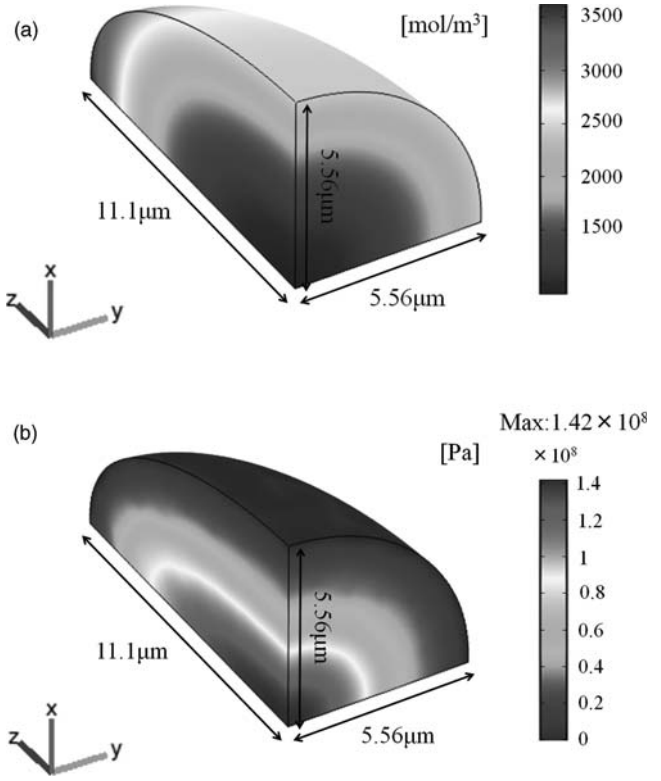


**Figure 6.** Lithium concentration profile and maximum principal stress in an ellipsoidal particle during the discharging process (aspect ratio = 2, charging rate = 0.35C, discharge time = 900 seconds when $\sigma_{1,MAX}$ peaks) (a) lithium concentration [mol/m$^3$] (b) max. principal stress [Pa].

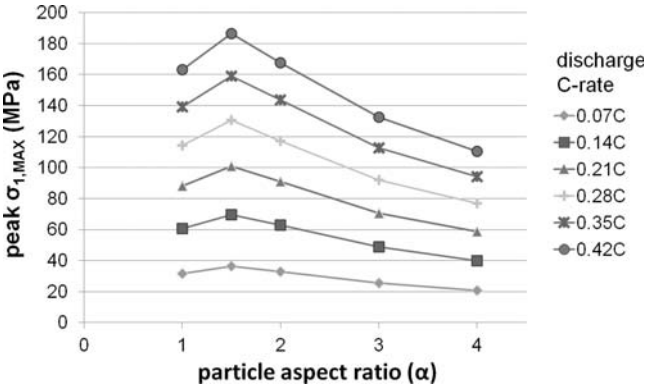


**Figure 7.** Peak $\sigma_{1,MAX}$ values with particle aspect ratio α. The particle volume was the same for all cases; and radius = 7 μm when α = 1.

circles represent all the simulation cases that have been performed; the green boundary separates the cases where crack propagation occurs from the cases where crack propagation does not occur; the simulation cases that are located closest to the boundary are marked with big blue dots (no crack propagation) and red diamonds (crack propagates). Additional simulations were performed with more refined current density increment (0.025 A/m$^2$) to provide a more accurate boundary.

*Particle aspect ratio.*— Figure 6a is a representation of the lithium concentration profile for an ellipsoidal particle when the stress level rises to its maximum during discharge. The highest level of lithium concentration can be found at the tip of the longer axes; however, the highest level of maximum principal stress is in the center of the particle, as shown in Fig. 6b. Under maximum principal stress fracture criterion, crack propagation was most likely to occur near the center of ellipsoidal particles. The $\sigma_{1,MAX}$ found in particles with different aspect ratios during discharge is plotted in Fig. 7. With increasing aspect ratio, the $\sigma_{1,MAX}$ in ellipsoidal particles first increased and then decreased at each C-rate. The highest value of $\sigma_{1,MAX}$ for the same C-rate can be found for particles with an aspect ratio of 1.5. The combination of particle aspect ratio and current level under which crack propagation occured for defects in the center of the particles was shown in Fig. 8. The critical boundary for crack propagation to occur was plotted in the same manner as in Fig. 5, which was described previously. From this boundary, particles with aspect ratio 1.5 were found to require the lowest discharge C-rate (about 0.18 C) for crack propagation to occur at the particle center.

*Initial defect location.*— Particles $4\pi \times (7\,\mu m)^3/3$ in volume and with aspect ratio 2 were used to determine the most favorable initial defect location for crack propagation. During the discharging process, when the initial crack was located at the center of the particle, crack propagation occured at a current rate of 0.21 C. The initial defect was moved along the semi-major axis and the C-rates at which fracture occurs were shown in Figure 9. When the defect was located away from the center by 1/3 or 1/2 of the length of the semi-major axis (position A and B), the crack propagated at a current rate of 0.28 C. A crack did not propagate even at 0.42 C in the case where the initial defect was located on the surface of the particle (position C). When the initial defect was then moved along the semi-minor axis away from the center by 1/3 the length of the semi-minor axis (position D), crack propagation occured at 0.35 C. When the initial defect was then moved along the semi-minor axis away from the center by 1/2 the length of the semi-minor axis (position E) or was located at the surface (Position F), crack propagation did not occur, even for discharging rates as high as 0.42 C. Fig. 9a shows the lowest C-rates at which fracture propagates for different initial defect locations. However, when the same particle was subjected to the charging process, an initial defect located in almost all of the above mentioned locations did not propagate for charging rates up to 0.42 C (except for Position F, the initial crack propagates at a charging rate of 0.35 C), as shown in Fig. 9b. Fig. 10 shows the lithium concentration level and the maximum principal stress level in the particle during the charging process. The $\sigma_{1,MAX}$ can be found at the surface of the particle corresponding to Position F. Comparing Fig. 9a and 9(b), it was noticed that crack propagation is most likely to occur from an initial defect at the center of the particle during discharge.

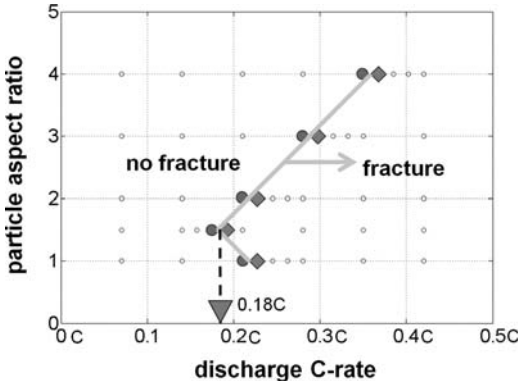


**Figure 8.** Fracture propagation conditions (aspect ratio and current density) with corresponding C-rates. Legend is the same as that of Fig. 5.

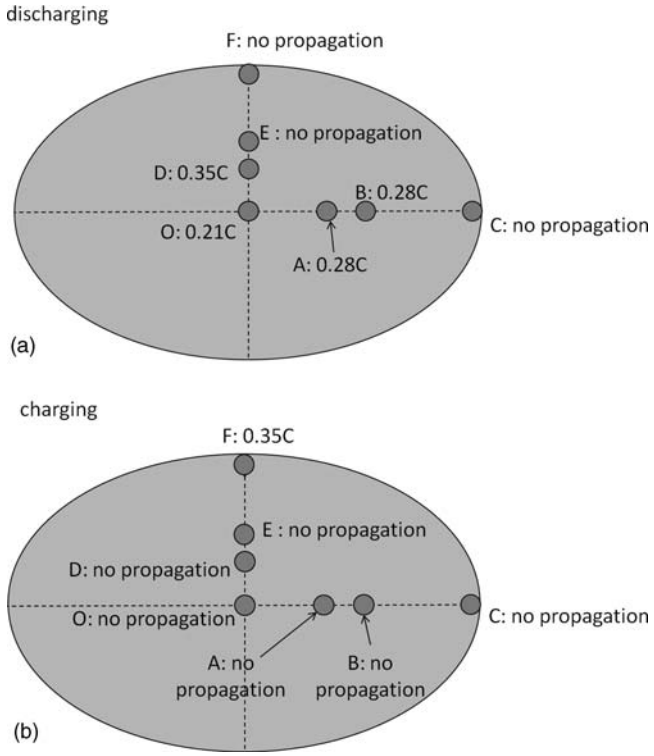


**Figure 9.** lowest C-rates (up to 0.42 C) at which fracture propagated for different initial defect location (a) during discharging; (b) during charging.

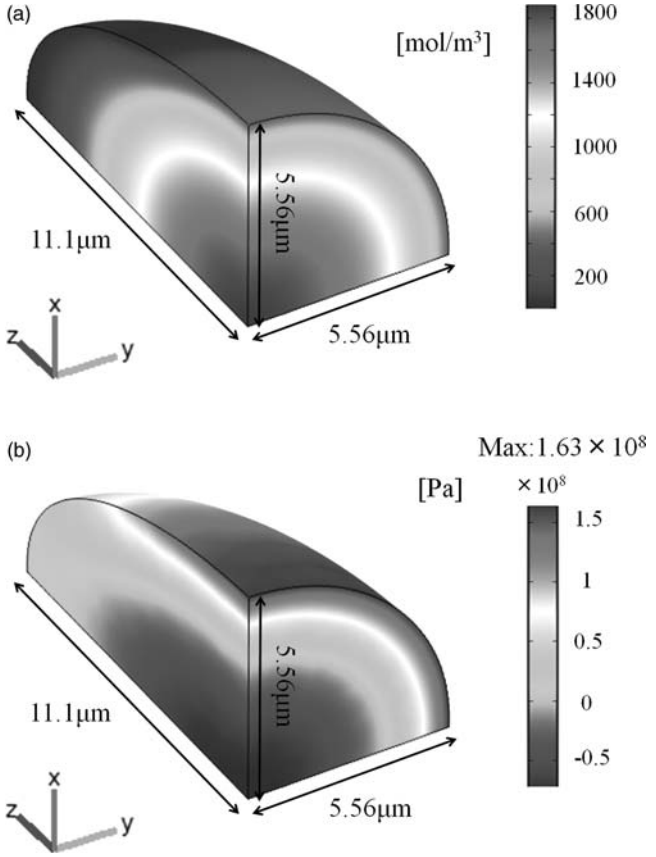


**Figure 10.** Lithium concentration profile and maximum principal stress during the charging process (aspect ratio = 2, charging rate = 0.35C, charge time = 10068 seconds when max. 1st principal stress reached the highest level) (a) lithium concentration [mol/m$^3$] (b) max. principal stress [Pa].

## Discussion

Only single smooth ellipsoidal particles were considered in this work; this was done to study the effect of parameters such as aspect ratio, particle size and current density, as well as the location of the initial defect. In the prior art, fracture mechanisms had been employed in electrode materials. However, in some cases realistic electrochemical loading conditions and the geometrical effects were not investigated[25]; in others, only perfectly spherical particles with initial defects located on the surface were considered.[26] Our findings—that fracture tends to propagate in particles with larger size and higher current density—are in agreement with the trend reported in these analysis results. However, due to differences in the parameters used, such as Young's Modulus, partial molar volume, and especially diffusivity (the reported diffusivity values from various sources has discrepancies of several orders of magnitudes), our results cannot be directly compared to the simulation results in the prior arts. While the prior arts generally consider spherical particles with initial defects located near the surface,[26] the efforts were focused on the propagation of initial defects inside the particle during the discharge of cathode materials, thus showing the energetically favorable location of crack propagation during cycling and revealing new possible ways of particle failure.

Our study shows that crack propagation can occur at a low C-rate at the order of C/5. This finding matches well with experimental observations of fracture in cathode active materials,[2,6] where cracking occurs when cycling at a rate of 30 mA/g (C/5) for LiFePO4 with a capacity of 149 mAh/g, and at a current density of 0.4 mA/cm$^2$ (also C/5) for $LiCoO_2$.

Even though the current simulations address some key physical phenomena related to fracture in the cathode particles, there are still issues important to understanding the entire mechanism of fracture in the active materials as well as the effect of fracture on battery performance. These topics include a wide range of physics; they cannot be addressed all together.

In this work only single isolated ellipsoidal particles were considered. The cathode system contains aggregated structures formed by active material particles, inactive polymer binder and conductive additive.[1] The interaction between multiple active material particles as well as interaction between different material phases will affect the stress level and the fracturing behavior of the particles as well as the integrity of the whole aggregated structure. It will be necessary not only to consider fracturing within the homogenous single phase, but also to investigate the disruption of the boundary between the active material and inactive material phases.[25]

Further, it was assumed that the cell was charged and discharged in the single phase region, and thus that Jahn-Teller distortion was prevented. Fig. 4 shows the dependence of maximum principal stress on the particle size and current density within this single phase region: larger particle size and higher current density will increase the level of maximum principal stress, thus increasing the chance for crack propagation to occur. In some real world applications, however, crystallites at the surface of the particle can be over-lithiated at high C-rates and undergo phase transition locally even when the overall voltage of the cell is above 3.0 V. This phase transition effect can lead to abrupt lattice parameter change and increase stress significantly when combined with volume change due to intercalation. This contributing factor to fracture propagation will be considered in a future study.

The present work considered smooth ellipsoidal particles. While these provide a more general representation of real world cathode particles than the purely spherical models, the present work should lead to the future simulation of particles with irregular shape and non-smooth multiple convex and concave surfaces, as well as with particles containing such defects as phase boundaries and/or grain boundaries. In addition, interaction between multiple particles as well as interaction between active material particles and polymer binders in the aggregates level of a cathode system should also be considered.

## Conclusions

In this work, multiphysics simulations and linear elastic fracture mechanics were employed to simulate crack propagation in ellipsoidal cathode particles under realistic electrochemical loading conditions.

It was found that a defect at the center of the particle will present the most adverse conditions in terms of failure through fracture during discharge. The maximum principal stress at particle center ranged from under 20 MPa to 200 MPa for particles with sizes from 3 $\mu$m to 9 $\mu$m and discharging current density from 0.1 A/m$^2$ to 0.6 A/m$^2$. The stress level in the most severe case was more than twice the maximum tensile strength. This resulted in crack propagation from the defect. It was also confirmed through simulation that an initial defect located at the center of the particle required the lowest C-rate to propagate during discharge, relative to other locations inside the particle or on the surface. The conditions that allowed such initial center defects in spherical and ellipsoidal particles to propagate were explored and mapped. Increasing particle size and current density contributed positively to the tendency of crack propagation. According to our results, for a spherical particle with a radius of 9 $\mu$m, a current density of more than 0.25 A/m$^2$ can lead to crack propagation, whereas a 4 $\mu$m-radius particle can withstand a current density of as high as 0.53 A/m$^2$ without failure through fracture.

However, the C-rates required for cracks to propagate decreased and then increased with increasing particle aspect ratio. For particles with an aspect ratio of about 1.5:1, the required C-rate for center defects to propagate was the lowest at 0.18 C.

Our simulation demonstrated that fracture can develop from defects under moderate C-rates. Thus, fracture effect should be considered in the design of batteries to minimize capacity degradation.

## Acknowledgments

This effort was supported by the Department of Energy, with additional sponsorship by the General Motors/University of Michigan Advanced Battery Coalition for Drivetrains. The authors appreciate the support from our sponsors.

## References

1. M. Zhu, J. Park, and A. M. Sastry, *Journal of The Electrochemical Society*, **158**(10), A1155 (2011).
2. D. Wang, X. Wu, Z. Wang, and L. Chen, *Journal of Power Sources*, **140**, 125 (2005).
3. A. Blyr, C. Sigala, G. Amatucci, D. Guyomard, Y. Chabre, and J. M. Tarascon, *Journal of The Electrochemical Society*, **145**(1), 194 (1998).
4. J. Park, J. H. Seo, G. Plett, W. Lu, and A. M. Sastry, *Electrochemical and Solid-State Letters*, **14**(2), A14 (2011).
5. M.-R. Lim, W.-I. Cho, and K.-B. Kim, *Journal of Power Sources*, **92**, 168 (2001).
6. H. Wang, Y.-I. Jang, B. Huang, D. R. Sadoway, and Y.-M. Chiang, *Journal of The Electrochemical Society*, **146**(2), 473 (1999).
7. M. M. Thackeray, Y. Shao-Horn, A. J. Kahaian, K. D. Kepler, E. Skinner, J. T. Vaughery, and S. A. Hackney, *Electrochem. Solid-State Lett.*, **1**(1), 7 (1998).
8. T. Ohzuku, M. Kitagawa, and T. Hirai, *J. Electrochem. Soc.*, **136**(11), 3169 (1989).
9. T. Ohzuku, H. Tomura, and K. Sawai, *J. Electrochem. Soc.*, **144**, 3496 (1997).
10. K. A. Striebel, A. Sierra, J. Shim, C.-W. Wang, and A. M. Sastry, *Journal of Power Sources*, **134**, 241 (2004).
11. C.-W. Wang, Y.-B. Yi, A. M. Sastry, J. Shim, and K. A. Striebel, *Journal of the Electrochemical Society*, **151**(9), 1489 (2004).
12. Y.-B. Yi, C.-W. Wang, and A. M. Sastry, *ASME Journal of Engineering Materials and Technology*, **128**(1), 73 (2006).
13. W. I. F. David, M. M. Thackeray, L. A. de Piccitotto, and J. B. Goodenough, *J. Solid State Chem.*, **67**, 316 (1987).
14. J. Scarminio, A. Talledo, A. A. Andersson, S. Passerini, and F. Decker, *Elecrrochimica Acta*, **38**(12), 1637 (1993).
15. T. Ohzuku, M. Kitagawa, and T. Hirai, *J. Electrochem. Soc.*, **136**(11), 3169 (1989).
16. T. Ohzuku, M. Kitagawa, and T. Hirai, *J. Electrochem. Soc.*, **137**, 769 (1990).
17. K. Zaghib, J. Shim, A. Guerfi, P. Charest, and K. A. Striebel, *Electrochem. Solid-State Lett.*, **8**, A207 (2005).
18. J. Christensen and J. Newman, *J. Solid State Electrochem.*, **10**, 293 (2006).
19. X. Zhang, W. Shyy, and A. M. Sastry, *Journal of The Electrochemical Society*, **154**(10), A910 (2007).
20. X. Zhang, A. M. Sastry, and W. Shyy, *Journal of the Electrochemical Society*, **155**(7), A542 (2008).
21. Y.-T. Cheng and M. W. Verbrugge, *J. Appl. Phys.*, **104**, 083521 (2008).
22. Y.-T. Cheng and M. W. Verbrugge, *J. Power Sources*, **190**, 453 (2009).
23. Y.-T. Cheng and M. W. Verbrugge, *Journal of The Electrochemical Society*, **157**(4), A508 (2010).
24. J. Christensen and J. Newman, *Journal of The Electrochemical Society*, **153**(6), A1019 (2006).
25. Y. Hu, X. Zhao, and Z. Suo, *J. Mater. Res.*, **25**(6), 1007 (2010).
26. W. H. Woodford, Y.-M. Chiang, and C. Carter, *Journal of The Electrochemical Society*, **157**(10), A1052 (2010).
27. S. Prussin, *J. Appl. Phys.*, **32**, 1876 (1961).
28. ABAQUS/Standard: Version 6.9. Hibbitt, Karlsson & Serensen, Inc. (2009).
29. J. Park, W. Lu, and A. M. Sastry, *Journal of The Electrochemical Society*, **158**(2), A201 (2011).
30. X. He, J. Cai, Y. Li, C. Jiang, and C. Wan, *Materials Chemistry and Physics*, **95**, 105 (2006).
31. T. H. Choa, S. M. Parka, M. Yoshioa, T. Hiraib, and Y. Hideshimab, *Journal of Power Sources*, **142**, 306 (2005).
32. A. Paolone, R. Cantelli, G. Rousse, and C. Masquelier, *J. Phys.: Condens. Matter*, **15**, 457 (2003).
33. A. Yoneda, *J. Phys. Earth*, **38**, 19 (1990).
34. D. Ravinder, *J. Appl. Phys.*, **75**, 6121 (1994).
35. F. Cardarelli, *Materials Handbook: A Concise Desktop Reference*, Springer-Verlag, London (2000).
36. A. Yamada and M. Tanaka, *Mater. Res. Bull.*, **30**, 715 (1995).